

2018

## High spatial resolution microdosimetry with monolithic Delta E-E detector on C-12 beam: Monte Carlo simulations and experiment

Linh T. Tran

*University of Wollongong*, tltran@uow.edu.au

David Bolst

*University of Wollongong*, dbolst@uow.edu.au

Susanna Guatelli

*University of Wollongong*, susanna@uow.edu.au

Giordano Biasi

*Politecnico di Milano*, gb446@uowmail.edu.au

Alberto Fazzi

*Politecnico di Milano*

*See next page for additional authors*

Follow this and additional works at: <https://ro.uow.edu.au/eispapers1>



Part of the [Engineering Commons](#), and the [Science and Technology Studies Commons](#)

### Recommended Citation

Tran, Linh T.; Bolst, David; Guatelli, Susanna; Biasi, Giordano; Fazzi, Alberto; Sagia, Elena; Prokopovich, Dale A.; Reinhard, Mark I.; Keat, Ying C.; Petasecca, Marco; Lerch, Michael L. F; Pola, A; Agosteo, Stefano; Matsufuji, Naruhiro; Jackson, Michael A.; and Rosenfeld, Anatoly B., "High spatial resolution microdosimetry with monolithic Delta E-E detector on C-12 beam: Monte Carlo simulations and experiment" (2018). *Faculty of Engineering and Information Sciences - Papers: Part B*. 1536.  
<https://ro.uow.edu.au/eispapers1/1536>

---

## High spatial resolution microdosimetry with monolithic Delta E-E detector on C-12 beam: Monte Carlo simulations and experiment

### Abstract

Nuclear fragmentation produced in  $^{12}\text{C}$  ion therapeutic beams contributes significantly to the Relative Biological Effectiveness (RBE)-weighted dose in the distal edge of the Spread out Bragg Peak (SOBP) and surrounding tissues in out-of-field. Complex mixed radiation field originated by the therapeutic  $^{12}\text{C}$  ion beam in a phantom is difficult to measure. This study presents a new method to characterise the radiation field produced in a  $^{12}\text{C}$  ion beam using a monolithic Delta E-E telescope which provides the capability to identify the particle components of the mixed radiation field as well as the microdosimetric spectra that allows derivation of the RBE based on a radiobiological model.

### Disciplines

Engineering | Science and Technology Studies

### Publication Details

Tran, L. T., Bolst, D., Guatelli, S., Biasi, G., Fazzi, A., Sagia, E., Prokopovich, D. A., Reinhard, M. I., Keat, Y. C., Petasecca, M., Lerch, M. L. F., Pola, A., Agosteo, S., Matsufuji, N., Jackson, M. & Rosenfeld, A. B. (2018). High spatial resolution microdosimetry with monolithic Delta E-E detector on C-12 beam: Monte Carlo simulations and experiment. *Nuclear Instruments and Methods in Physics Research Section A: Accelerators, Spectrometers, Detectors, and Associated Equipment*, 887 70-80.

### Authors

Linh T. Tran, David Bolst, Susanna Guatelli, Giordano Biasi, Alberto Fazzi, Elena Sagia, Dale A. Prokopovich, Mark I. Reinhard, Ying C. Keat, Marco Petasecca, Michael L. F. Lerch, A. Pola, Stefano Agosteo, Naruhiro Matsufuji, Michael A. Jackson, and Anatoly B. Rosenfeld

# High spatial resolution microdosimetry with monolithic $\Delta E$ -E detector on $^{12}\text{C}$ beam: Monte Carlo simulations and Experiment.

Linh T. Tran<sup>1</sup>, David Bolst<sup>1</sup>, Susanna Guatelli<sup>1</sup>, Giordano Biasi<sup>4</sup>, Alberto Fazzi<sup>4</sup>, Eleni Sagia<sup>4</sup>, Dale A. Prokopovich<sup>2</sup>, Mark I. Reinhard<sup>2</sup>, Ying C. Keat<sup>3</sup>, Marco Petasecca<sup>1</sup>, Michael L. F. Lerch<sup>1</sup>, Andrea Pola<sup>4</sup>, Stefano Agosteo<sup>4</sup>, Naruhiro Matsufuji<sup>5</sup>, Michael Jackson<sup>6</sup> and Anatoly B. Rosenfeld<sup>1</sup>

<sup>1</sup>Centre for Medical Radiation Physics, University of Wollongong, NSW 2522, Australia

<sup>2</sup>NSTLI Nuclear Stewardship, Australian Nuclear Science and Technology Organization, Lucas Heights, NSW 2234, Australia

<sup>3</sup>University Sains Malaysia, Pulau Penang, Malaysia

<sup>4</sup>Dipartimento di Ingegneria Nucleare, Politecnico di Milano, 20133 Milano, Italy

<sup>5</sup>Research Centre for Charge Particle Therapy, National Institute of Radiological Science, Chiba, Japan

<sup>6</sup>University of New South Wales, Sydney NSW 2052, Australia

E-mail: anatoly@uow.edu.au

**Abstract.** Nuclear fragmentation produced in  $^{12}\text{C}$  ion therapeutic beams contributes significantly to the Relative Biological Effectiveness (RBE) - weighted dose in the distal edge of the Spread out Bragg Peak (SOBP) and surrounding tissues in out-of-field. Complex mixed radiation field originated by the therapeutic  $^{12}\text{C}$  ion beam in a phantom is difficult to measure. This study presents a new method to characterise the radiation field produced in a  $^{12}\text{C}$  ion beam using a monolithic  $\Delta E$ -E telescope which provides the capability to identify the particle components of the mixed radiation field as well as the microdosimetric spectra that allows derivation of the RBE based on a radiobiological model. The response of the monolithic  $\Delta E$ -E telescope to a 290 MeV/u  $^{12}\text{C}$  ion beam at defined positions along the pristine Bragg Peak was studied using the Geant4 Monte Carlo toolkit. The microdosimetric spectra derived from the  $\Delta E$  stage and the two-dimensional scatter plots of energy deposition in  $\Delta E$  and E stages of the device in coincidence are presented, as calculated in-field and out-of-field. Partial dose weighted contribution to the microdosimetric spectra from nuclear fragments and recoils, such as  $^1\text{H}$ ,  $^4\text{He}$ ,  $^3\text{He}$ ,  $^7\text{Li}$ ,  $^9\text{Be}$  and  $^{11}\text{B}$ , have been analyzed for each position. Comparison of simulation and experimental results are presented and demonstrates that the microdosimetric spectra changes dramatically within 0.5 mm depth increments close to and at the distal edge of the Bragg Peak which is impossible to identify using conventional Tissue Equivalent Proportional Counter (TEPC).

## 1. Introduction

Charged particle therapy with  $^{12}\text{C}$  ions has the advantage over X-ray radiotherapy due to the Bragg Peak (BP) producing a highly conformal dose profile. Charged particle therapy is normally used for the treatment of deep-seated tumours while preserving the surrounding healthy tissues. The energy deposition mechanism of ions in matter is dominated by the electronic collisions for the relevant energies of primary ion, described by Bethe-Bloch formula [1, 2]. The nuclear reactions contribute substantially to the ion dose via nuclear fragmentation and neutrons production. The determination of the Relative Biological Effectiveness (RBE) is crucial for particle therapy, particularly for heavier ions such as  $^{12}\text{C}$ , as the biological dose is required as a parameter in patient treatment planning. Accurate knowledge of the RBE in-field and out-of-field is essential for determining the physical dose at a

50 particular depth,  $D$ , to have the biological dose (RBED) constant along the SOBP, and to evaluate the  
 51 secondary cancer risk and biological dose at Organs At Risk (OAR) out of the treatment field.

52 The RBE of a  $^{12}\text{C}$  therapeutic beam changes dramatically with depth, especially towards the end of  
 53 the Bragg Peak (BP) due to the very high Linear Energy Transfer (LET) of the  $^{12}\text{C}$  ions in this region  
 54 [3]. Additional complexity in the determination of the RBE in the target is associated with the nuclear  
 55 fragmentation process in the SOBP.  $^{12}\text{C}$  fragmentation produces lighter charged ions with lower LET  
 56 than for primary  $^{12}\text{C}$  ions as well as neutrons, which results in a slight reduction of the primary  $^{12}\text{C}$   
 57 ions with increasing of the depth, as well as the production of a mixed radiation field which causes a  
 58 low dose “tail” that extends beyond the distal edge of the SOBP [4]. The shape of the SOBP is formed  
 59 by means of multiple pristine  $^{12}\text{C}$  Bragg Peaks, which result in the formation of RBE ripples along the  
 60 plateau of the SOBP.

61 An effective approach to derive the RBE for a  $^{12}\text{C}$  ion beam is microdosimetry [5]. The  
 62 microdosimetric approach involves measuring the frequency  $f(y)$  of the stochastic lineal energy  
 63 deposition  $y$ , in a micron sized tissue equivalent sensitive volume (SV). The lineal energy deposition  $y$   
 64 is defined as:

$$y = \frac{E}{\langle l \rangle}, \quad (1)$$

65 where  $E$  is the energy deposition in the SV, which has an average chord length  $\langle l \rangle$ . Once the  
 66 microdosimetric spectra  $y^2 f(y)$  vs  $y$  of a radiation field in tissue equivalent material is known, the RBE  
 67 can be derived based on the modified microdosimetric-kinetic model (MKM) [6]. The  $\text{RBE}_{10}$  of the  
 68  $^{12}\text{C}$  ion beam is defined as the ratio of the dose required to achieve 10% cell survival using X-rays to  
 69 that required when using the radiation of interest:

$$\text{RBE}_{10} = \frac{2\beta D_{10,R}}{\sqrt{\alpha^2 - 4\beta \ln(0.1)} - \alpha}, \quad (2)$$

70 where  $\alpha$ ,  $\beta$  are individual tissue radiosensitivity coefficients ( $\alpha$ , in units of  $\text{Gy}^{-1}$  and  $\beta$ , in units of  $\text{Gy}^{-2}$ )  
 71 determined the cell survival,  $D_{10,R} = 5.0 \text{ Gy}$  is the dose corresponding to 10% survival for human  
 72 salivary gland (HSG) cells using 200 kVp X-rays as reference radiation.  $\alpha$  is defined as:

$$\alpha = \alpha_0 + \frac{\beta}{\rho \pi r_d^2} y^*, \quad (3)$$

73 where  $\alpha_0 = 0.13 \text{ Gy}^{-1}$  is a constant that represents the initial slope of the survival fraction curve in the  
 74 limit of zero LET,  $\beta = 0.05 \text{ Gy}^{-2}$  is a constant independent of LET,  $\rho = 1 \text{ g/cm}^3$  is the density of  
 75 tissue and  $r_d = 0.42 \text{ }\mu\text{m}$  is the radius of a sub-cellular domain in the MK model.

$$y^* = \frac{y_0^2 \int_0^\infty (1 - \exp(-y^2/y_0^2)) f(y) dy}{\int_0^\infty y f(y) dy}, \quad (4)$$

76 where  $y_0 = 150 \text{ keV}/\mu\text{m}$  is used in this study in order to match the calculation method used at the  
 77 Heavy Ion Medical Accelerator in Chiba (HIMAC) in experiments with the tissue equivalent  
 78 proportional counter (TEPC).

79 The Centre for Medical Radiation Physics (CMRP), University of Wollongong, has initiated the  
 80 concept of silicon microdosimetry to replace the current microdosimetry gold standard, the TEPC.  
 81 Compared to the TEPC, silicon microdosimeters are advantageous due to being a solid-state detector  
 82 with no gas-flow ensemble, having very low operating voltages less than 10 V, extremely high spatial  
 83 resolution ( $\mu\text{m}$  scale) and a high degree of portability. Current status of silicon microdosimetry can be  
 84 found elsewhere [7].

85 The characteristics of secondary charged particles in  $^{12}\text{C}$  ion beams of 200 and 400 MeV/u have  
 86 been previously studied using the combination of energy loss and time-of-flight (TOF) measurements.  
 87 A thin scintillation paddle with 1.5 mm thick coupled to a Hamamatsu photomultiplier tube was used  
 88 [8]. The monolithic  $\Delta E$ -E telescope with 1.8  $\mu\text{m}$  thick  $\Delta E$  stage can be used at the same time as a  
 89 microdosimeter and as detector to identify products deriving from nuclear fragmentation [9, 10].

90 The latest design of the monolithic telescope has a pixelated  $\Delta E$  detector with SVs similar in  
91 geometry to CMRP SOI microdosimeters [7, 11]. The pixelated  $\Delta E$  stage allows the device to be used  
92 as a microdosimeter while also providing particle identification [12].

93 The  $\Delta E$ -E telescope was used earlier to derive the RBE based on the microdosimetric approach, at  
94 defined positions along and downstream of a 100 MeV pristine proton Bragg peak and including distal  
95 part of SOBP at the proton therapy facility at Loma Linda University [13]. It was demonstrated that  
96 the maximum RBE value did not coincide with the physical dose peak position but was slightly  
97 downstream of the distal edge of the Bragg Peak. The study showed that the RBE varied with the  
98 depth along the SOBP and was higher than the RBE value being used in proton treatment planning  
99 (equal to a constant value of 1.1 along the SOBP). This was in agreement with currently published  
100 experimental microdosimetry based derived RBE obtained with high spatial resolution in therapeutic  
101 proton beams [14].

102 We are currently investigating the use of the  $\Delta E$ -E monolithic telescope for RBE determination  
103 both in-field and out-of-field of the  $^{12}\text{C}$  ion beam field. The project involved experimental  
104 characterisation of the device at the HIMAC facility, Chiba, Japan, coupled with Geant4-based  
105 simulation studies.

106 In this paper we present the response of the  $\Delta E$ -E telescope in-field and out-of-field of a 290  
107 MeV/u  $^{12}\text{C}$  beam simulated by Geant4 to justify application of the  $\Delta E$ -E telescope as a high spatial  
108 resolution Quality Assurance (QA) tool in heavy ion therapy (HIT). The simulation results are  
109 compared to experimental measurements performed at HIMAC, to have a first indication on the  
110 accuracy of the Geant4 simulation model. Particular attention was devoted to the study of the  $^{12}\text{C}$   
111 fragmentation and neutrons contribution to the derived RBE in the distal part and downstream of the  
112 Bragg peak.

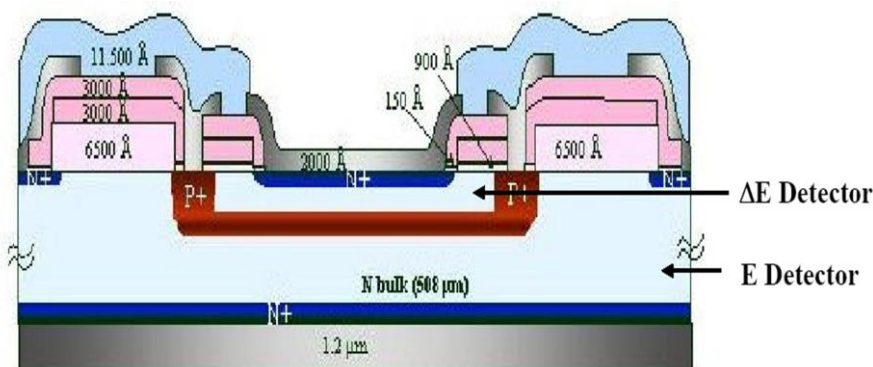
## 113 2. Materials and Methods

### 114 2.1 $\Delta E$ -E Telescope System Description.

115 The monolithic  $\Delta E$ -E monolithic telescope, manufactured at ST Microelectronics (Catania, Italy),  
116 consists of a 1.8  $\mu\text{m}$   $\Delta E$  and a 500  $\mu\text{m}$  E thick stage, both manufactured on a single silicon substrate.  
117 The detector response can be presented as a two-dimensional scatter plot of the  $\Delta E$  vs  $\Delta E + E$  energy  
118 deposition via coincidence data acquisition.

119 A schematic of the  $\Delta E$ -E telescope is shown in Fig. 1, where thin metallised  $\text{N}^+$  implanted n-p  
120 junctions for both  $\Delta E$  and E detectors are depleted towards a  $\text{P}^+$  buried anode which is a common  
121 ground contact separating the two stages of the detector. To fully deplete the particle telescope the  $\text{N}^+$   
122 contact  $\Delta E$  was biased at +5 V and the  $\text{N}^+$  contact of the E stage was biased at +100 V relative to the  
123  $\text{P}^+$  buried layer.

124 The  $\Delta E$ -E particle telescope can be operated in a number of modes by utilizing the  $\Delta E$  and E  
125 detectors separately or in coincidence. When operated separately, the  $\Delta E$  detector acts like a  
126 microdosimeter in the case when the charged particle beam is normally incident to the surface of the  
127 detector. The mean chord length is defined by the thickness of the  $\Delta E$  detector (1.8  $\mu\text{m}$ ) for normally  
128 incident radiation.



129  
130 **Figure 1.** Schematic of  $\Delta E$ -E telescope. Figure adapted from [14].  
131

132 2.2 *Geant4 Simulation Application*

133 The Geant4 version 4.9.6.p01 [15] was used to model the radiation field and the response of the  
 134  $\Delta E$ -E telescope to a 290 MeV/u  $^{12}\text{C}$  beam in a PMMA phantom.

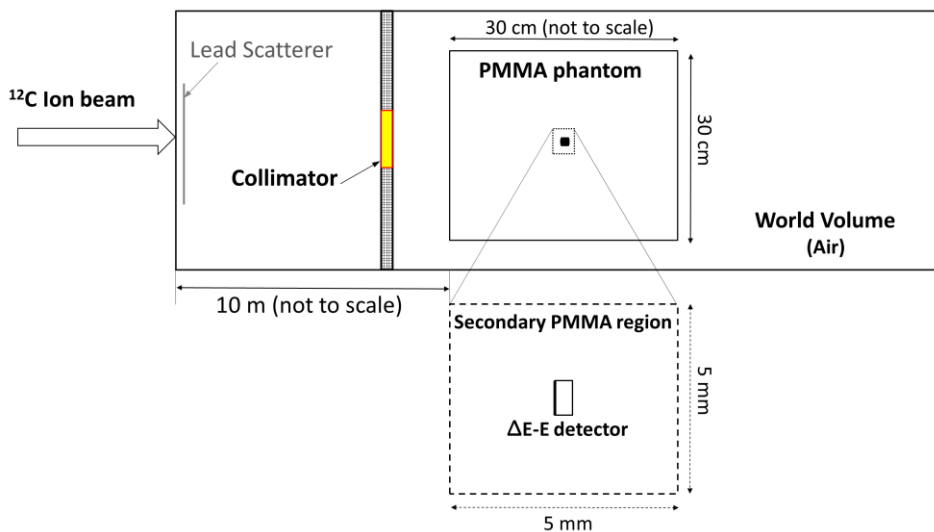
135 The experimental setup of the simulation, illustrated in Figure 2, reflected the experimental  
 136 conditions of the measurements performed at HIMAC. The  $^{12}\text{C}$  ion beam was simulated with an area  
 137 of  $1 \times 1 \text{ mm}^2$  and the distance from the ion beam line exit window to the surface of the phantom was  
 138 10 m as shown in Fig. 2. A 0.4 mm thick lead scatterer, placed at 5 mm from the ion beam line exit  
 139 window, was used for beam scattering. A 50 mm thick brass collimator with  $10 \times 10 \text{ cm}^2$  square  
 140 aperture was placed at 30 cm from the surface of the phantom. The mixed radiation field produced by  
 141 the incident  $^{12}\text{C}$  ion beam was studied in the PMMA phantom, modelled as a  $30 \times 30 \times 30 \text{ cm}^3$  box,  
 142 with elemental composition taken from ICRU [16] and with a density of  $1.17 \text{ g/cm}^3$ .

143 The electromagnetic interactions of particles were described by means of the Geant4 Standard  
 144 Physics Package (*G4EmStandardPhysics\_option3*). The hadronic interactions were described by  
 145 means of the *QGSP\_BIC\_HP* physics list. Ion nuclear interactions were modeled with the  
 146 *G4IonBinaryCascadeModel*.

147 In the first part of the study, the mixed radiation field deriving from the  $^{12}\text{C}$  ion beam was  
 148 characterised. The output of the simulation consisted of the energy deposition in the PMMA phantom  
 149 as well as the position of secondary particles generated within the phantom. The energy deposition  
 150 derived from the incident primary beam and from the secondary nuclear fragments was tallied  
 151 separately. The Bragg Peak was calculated along the direction of the incident beam with 0.1 mm  
 152 spatial resolution. The deposited energy at a given depth on a beam central axis and laterally was  
 153 stored in the 2D histogram which had  $1 \text{ mm}^2$  pixels.

154 In the second part of the study, the response of the  $\Delta E$ -E telescope to a 290 MeV/u  $^{12}\text{C}$  beam was  
 155 modelled to verify the capability of this device in identifying different nuclear fragments in-field and  
 156 out-of-field.

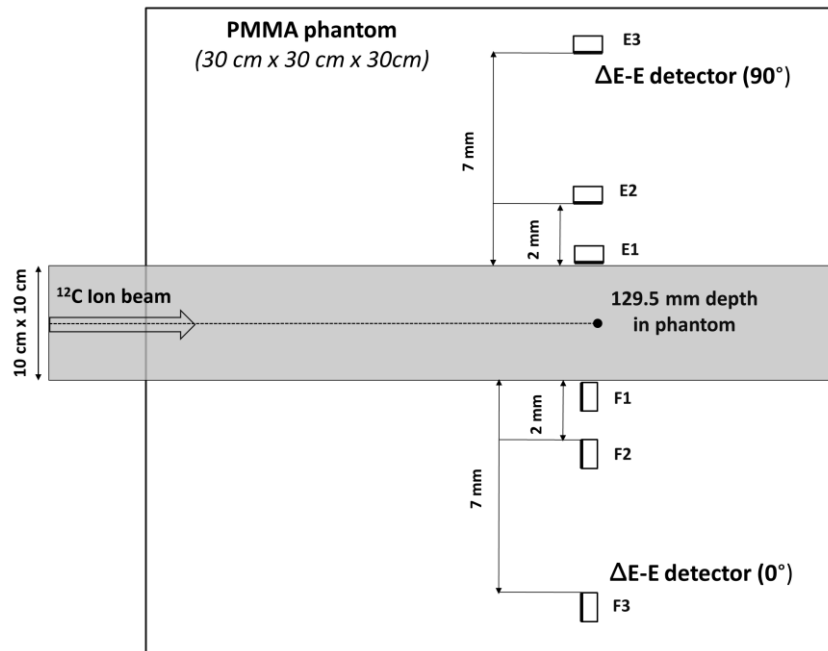
157 The geometry of the  $\Delta E$  and E stages was modelled as  $1 \text{ mm} \times 1 \text{ mm} \times 1.8 \text{ }\mu\text{m}$  and  $1 \text{ mm} \times 1 \text{ mm} \times$   
 158  $500 \text{ }\mu\text{m}$  silicon slabs. The  $\Delta E$ -E telescope was placed in the PMMA phantom at different depth. The  
 159 Geant4 *cuts per region* [17] were used to reduce the simulation times without affecting the accuracy of  
 160 the results. The size of the region was chosen based on a conservative consideration of the range of  
 161 secondary electrons produced by the primary  $^{12}\text{C}$  ion beam field. The maximum range of delta  
 162 electrons produced by a 290 MeV/u  $^{12}\text{C}$  was approximately 2.4 mm in PMMA (NIST database [18]).  
 163 Based on these considerations the region was centred with the detector, with a lateral size of 5 mm to  
 164 track all  $\delta$ -electrons at the required accuracy in the surrounding  $\Delta E$ -E telescope. The range cut was set  
 165 low enough to track the  $\delta$ -electrons down to the low energy limit of the Geant4 Standard  
 166 Electromagnetic Physics of 1 keV. Outside the region, the cut was set to 2 mm to reduce computation  
 167 time because those  $\delta$ -electrons with a range smaller than 2 mm cannot reach the  $\Delta E$ -E telescope.



168 **Figure 2.** Schematic representation of the simulated geometry of  $\Delta E$ -E telescope in the Geant4 simulation.  
 169

170 Fig. 2 shows the simulated experimental set-up. The energy deposition was calculated per incident  
 171 particle on the device, depositing energy in both  $\Delta E$  and E stages (coincidence mode). The energy  
 172 deposition caused by  $\delta$ -electrons and other secondary particles originating inside the two detector  
 173 stages was assigned to the parent particle incident on the device. The kinetic energy, charge, and  
 174 baryon number of the particle producing the energy deposition event in the device were scored.

175 The in-field and out-of-field response of the  $\Delta E$ -E telescope was obtained at 15 positions along the  
 176 axis of irradiation, that is: 0, 10, 58, 106, 125, 126.5, 127, 128, 128.5, 129.5, 130, 131.5, 136.5, 141,  
 177 and 155 mm. These positions were selected to encompass both in-field and downstream of the Bragg  
 178 Peak measurements as well as to match the experimental measurement positions.



179  
 180 **Figure 3.** Schematic representation of out of field positions of the  $\Delta E$ -E telescope in the Geant4 simulations and  
 181 experiments (not to scale). Positions F4 and E4 corresponding to 47 mm lateral distance from the edge of the  
 182 radiation field are not shown due to space limitation.  
 183

184 The out-of-field response of the  $\Delta E$ -E telescope was studied to characterise composition of the  
 185 mixed radiation field, including the scattered primary ion beam, fragments and neutrons which are  
 186 needed to estimate the stochastic probability of secondary cancer induction. The out-of-field study was  
 187 done with the  $\Delta E$ -E telescope facing the  $^{12}\text{C}$  ion beam (face on  $0^\circ$ ) and edge on ( $90^\circ$ ) as shown in Fig.  
 188 3. The  $\Delta E$ -E telescope was placed at 0 mm, 2 mm, 7 mm and 47 mm laterally from the edge of the  
 189 radiation field at the Bragg Peak region (for both cases: “face on” noted as F and “edge on” noted as  
 190 E).

### 191 3. Results and discussion

#### 192 3.1 Characterisation of $^{12}\text{C}$ ion beam mixed radiation field

193 Fig. 4a shows the energy deposited by the incident 290 MeV/u  $^{12}\text{C}$  ions and by the secondary  
 194 fragment particles. A Bragg Peak was observed at  $(129.5 \pm 0.1)$  mm in the PMMA phantom which  
 195 agrees with calculated results by SRIM [19]. The main contribution to the total energy deposition  
 196 derived from the incident  $^{12}\text{C}$  ion beam, fragments, neutrons and the secondary carbon ions. Secondary  
 197 carbon ions resulted mostly from neutron elastic scattering within the PMMA. Such secondary carbon  
 198 ions are absent in the case of a water phantom. The peak of the secondary carbon ion appeared at 120  
 199 mm in the PMMA phantom (Fig. 4b). Contributions to the total energy deposition were seen from  
 200 secondary nuclei, due to recoils, namely H, He, Li, Be, B, N, and O. The almost negligible energy  
 201 deposition contributed by N and O was not included in Fig. 4b.

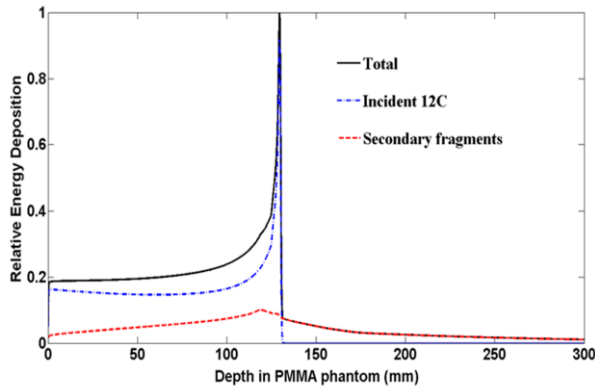


**Figure 4a.** Dose per incident  $^{12}\text{C}$  ion. The contribution deriving from incident  $^{12}\text{C}$  ions and secondary fragments are shown in blue and red, respectively. The sum of the two contributions is shown with the black curve. The energy deposition at the BP was normalised to 1.

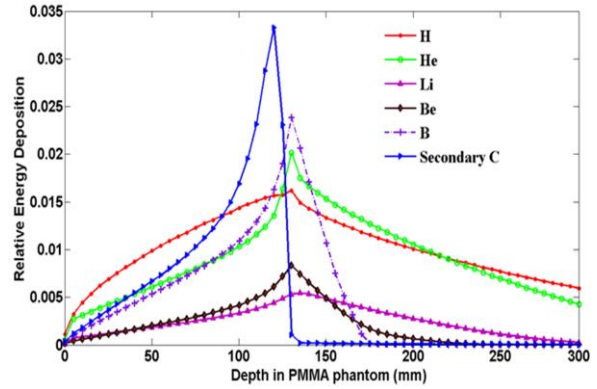


**Figure 4b.** Energy deposition deriving from the most significant secondary nuclear fragments and recoil secondary carbon ions (non-primary carbon ions). The total energy deposited by the secondary fragments component was normalised to 1.

202

**Table 1.** Number of secondary particles produced per single incident  $^{12}\text{C}$  ion

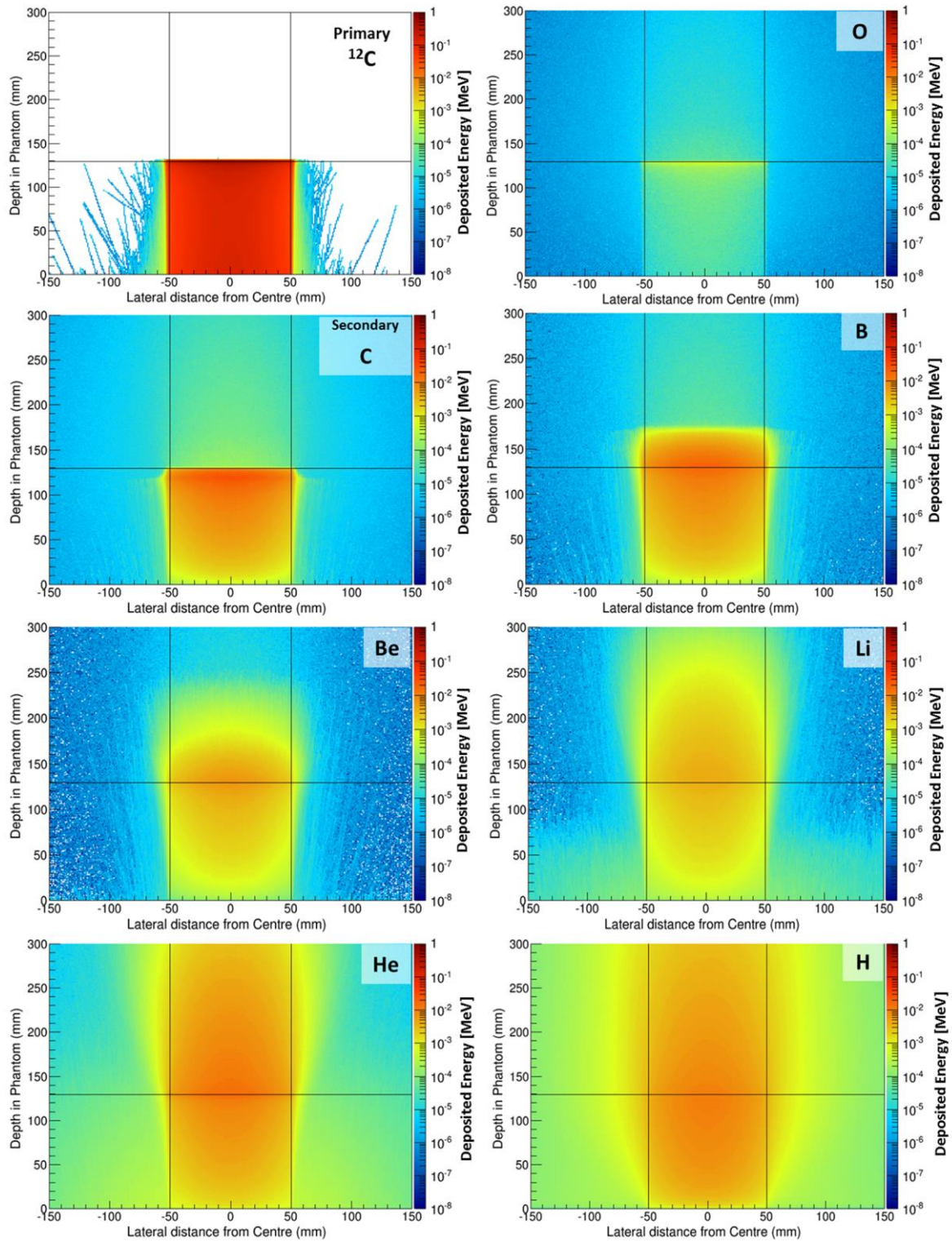
Particle	Production per single $^{12}\text{C}$
H	25.33
Secondary C	4.26
Neutron	2.37
O	1.48
He	1.29
B	0.49
Li	0.24
N	0.16
Be	0.14

203 Table 1 shows the number of secondary fragments generated per single incident  $^{12}\text{C}$  ion and  
 204 indicate that protons possess the highest yield. These protons are fragmented protons as well as recoil  
 205 protons generated in elastic reactions when the neutrons interacted with the hydrogen nuclei in the  
 206 PMMA material. The second largest secondary particle yield was from secondary C followed by  
 207 neutron, O, He, B, Li, N and Be ions.

208 Fig. 5 shows the 2D energy distribution from primary and secondary particles in the PMMA  
 209 phantom. Two additional lines were added to mark the edges of the primary beam (10 cm x 10 cm)  
 210 and range of the primary carbon ions. The 2D histogram shows the minimal scattering of the primary  
 211  $^{12}\text{C}$  ions outside the radiation field that confirm the advantage of HIT with a sharp penumbra. All  
 212 fragmented ions are producing dose buildup towards the end of the Bragg peak as demonstrated in  
 213 Figs 4b and 5. Fragmented C, O, B, Be and Li ions are mostly forward scattered while H and He ions  
 214 are producing essential dose halo laterally and downstream of the Bragg peak. It is worth to mention  
 215 that the maximum of deposited energy from H, B and He ions is slightly shifted forward in  
 216 comparison to the Bragg Peak of primary C ions.

217



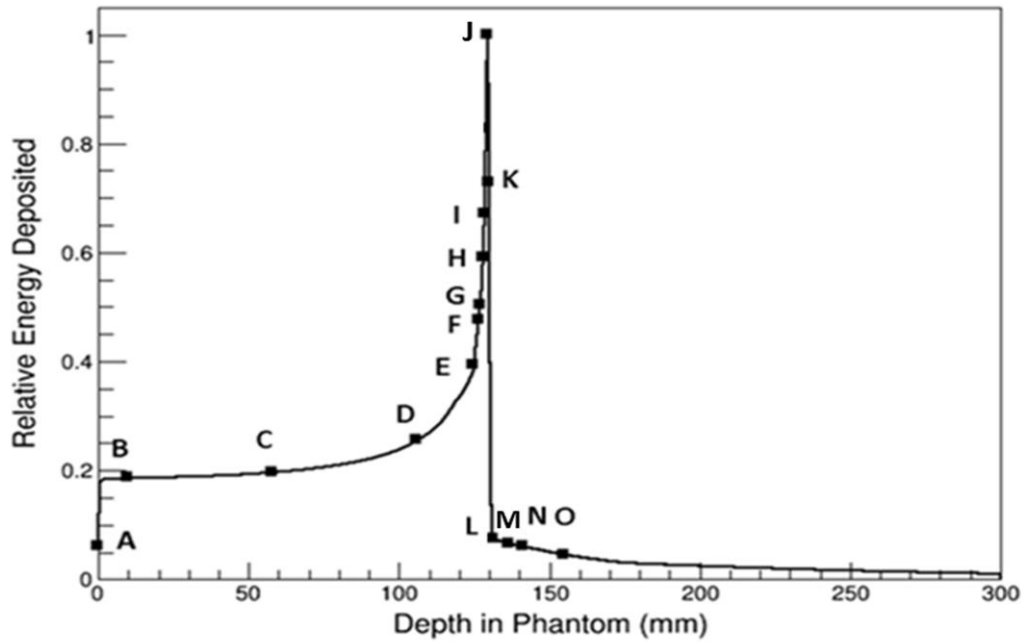


218

219 **Figure 5.** 2D energy deposition map of primary and secondary particles in the PMMA phantom for HIMAC  
 220 experiment set up. The results are shown per incident particle.

221 *3.2 Characterisation of the  $\Delta E$ -E telescope response in-field*

222 Fig. 6 shows the positions (A-O) along the 290 MeV/u  $^{12}\text{C}$  ion beam Bragg Peak, where the  $\Delta E$ -E  
 223 telescope was set.



224

225 **Figure 6.** A-O points indicate the positions along the 290MeV/u  $^{12}\text{C}$  Bragg Peak where the  $\Delta\text{E}$ -E  
 226 telescope was set.

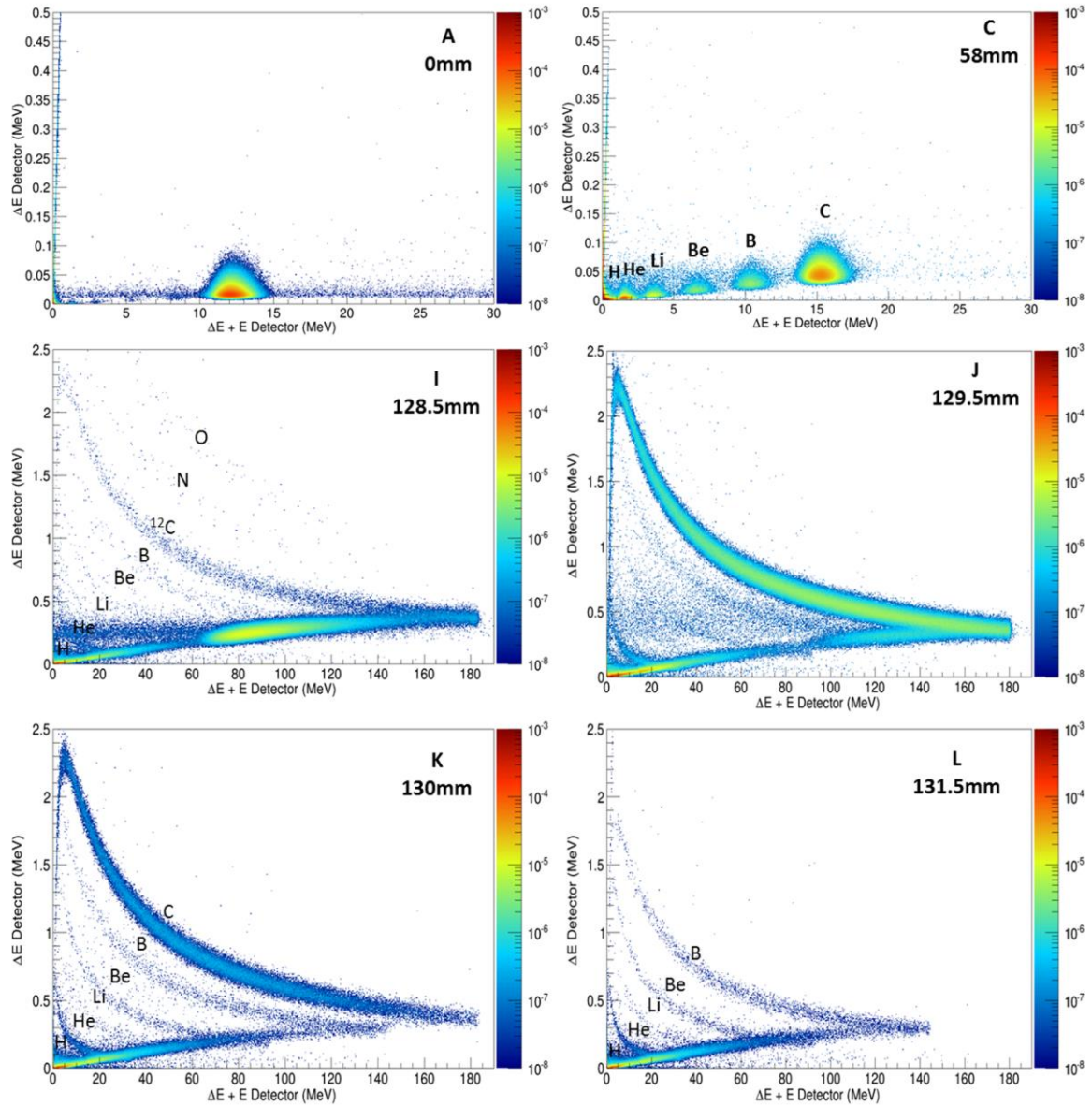
227 The coincident signals from the  $\Delta\text{E}$  and E detectors in response to the 290 MeV/u  $^{12}\text{C}$  beam were  
 228 mapped in a two dimensional (2D) scatter plot as  $\Delta\text{E}$  vs  $\Delta\text{E}+\text{E}$ . Fig. 7 shows the simulated 2D ( $\Delta\text{E}$ ,  
 229  $\text{E}+\Delta\text{E}$ ) scatter plots at positions A, C, I, J, K, L, which correspond to 0 mm, 58 mm, 128.5 mm, 129.5  
 230 mm, 130 mm and 131.5mm depths within the PMMA phantom. The  $\Delta\text{E}$ -E detector was placed along  
 231 the central axis of the beam. It can be seen that at 0 mm depth in the phantom, 290 MeV/u  $^{12}\text{C}$  ions  
 232 completely traversed the  $\Delta\text{E}$  and E stages. The majority of energy events deposited in the E stage  
 233 ranged between 11-13MeV. Events occurred in  $\Delta\text{E}$  stage are due to electrons which are traveling  
 234 essentially along the  $\Delta\text{E}$  detector and then scattered to E detector. The events along horizontal line  
 235 depositing approximately 0.01-0.02MeV in the  $\Delta\text{E}$  stage are due to primary  $^{12}\text{C}$  ions crossing through  
 236 the  $\Delta\text{E}$  and E stage of the detector under different angles.

237 At a depth of 58 mm in the PMMA phantom, the energy deposition regions corresponding to B, Be,  
 238 Li, He, H fragments are clearly visible in the scatter plot.

239 At 128.5 mm depth in the PMMA phantom, the loci corresponding to fragmentation products are  
 240 clearly observed. The maximum energy deposited in the E stage is about 185 MeV, which corresponds  
 241 to the energy of  $^{12}\text{C}$  ion having a range in silicon equal to the thickness of E stage of 500  $\mu\text{m}$ . The  
 242 energy deposited in the  $\Delta\text{E}$  stage for 185 MeV  $^{12}\text{C}$  ion is approximately 0.4 MeV. Events on a scatter  
 243 plot on the left of the kink with an increased energy deposited in  $\Delta\text{E}$  stage are corresponding to  
 244 stoppers in the E stage. The most frequent energy deposition events occur between 80 and 100 MeV in  
 245 the E stage which means that the majority of primary carbon ions are crossers as this depth while  
 246 straggled essentially. The loci corresponding to oxygen and nitrogen were observed and corresponded  
 247 to particles produced by inelastic reactions when  $^{12}\text{C}$  ions interacted-with the PMMA phantom.

248 The 2D energy scatter plot simulated in the  $\Delta\text{E}$ -E telescope placed at the pinnacle of the Bragg  
 249 peak (position J at 129.5 mm) is shown in Fig. 7. While most primary C ions are stoppers in E stage  
 250 some of the C ions are still crossers due to increased straggling at the end of the range.

251 At 130 mm depth, the C ion locus is without a lower part of the kink due to all  $^{12}\text{C}$  ions stopping  
 252 within the E stage with a maximum energy of 2.4MeV in the  $\Delta\text{E}$  stage. Multiple loci that  
 253 corresponded to the detection of different types of fragmented ions such as B, Be, Li, He, H were  
 254 clearly seen. At a depth of 131.5 mm the contribution of all fragmentation was still observed These  
 255 results show that in principle the  $\Delta\text{E}$ -E detector is suitable for  $^{12}\text{C}$  ion beam radiation field  
 256 characterisation with high spatial resolution in the distal edge of the Bragg peak providing accurate  
 257 information at what depth the deposited energy is due to fragments only.



258

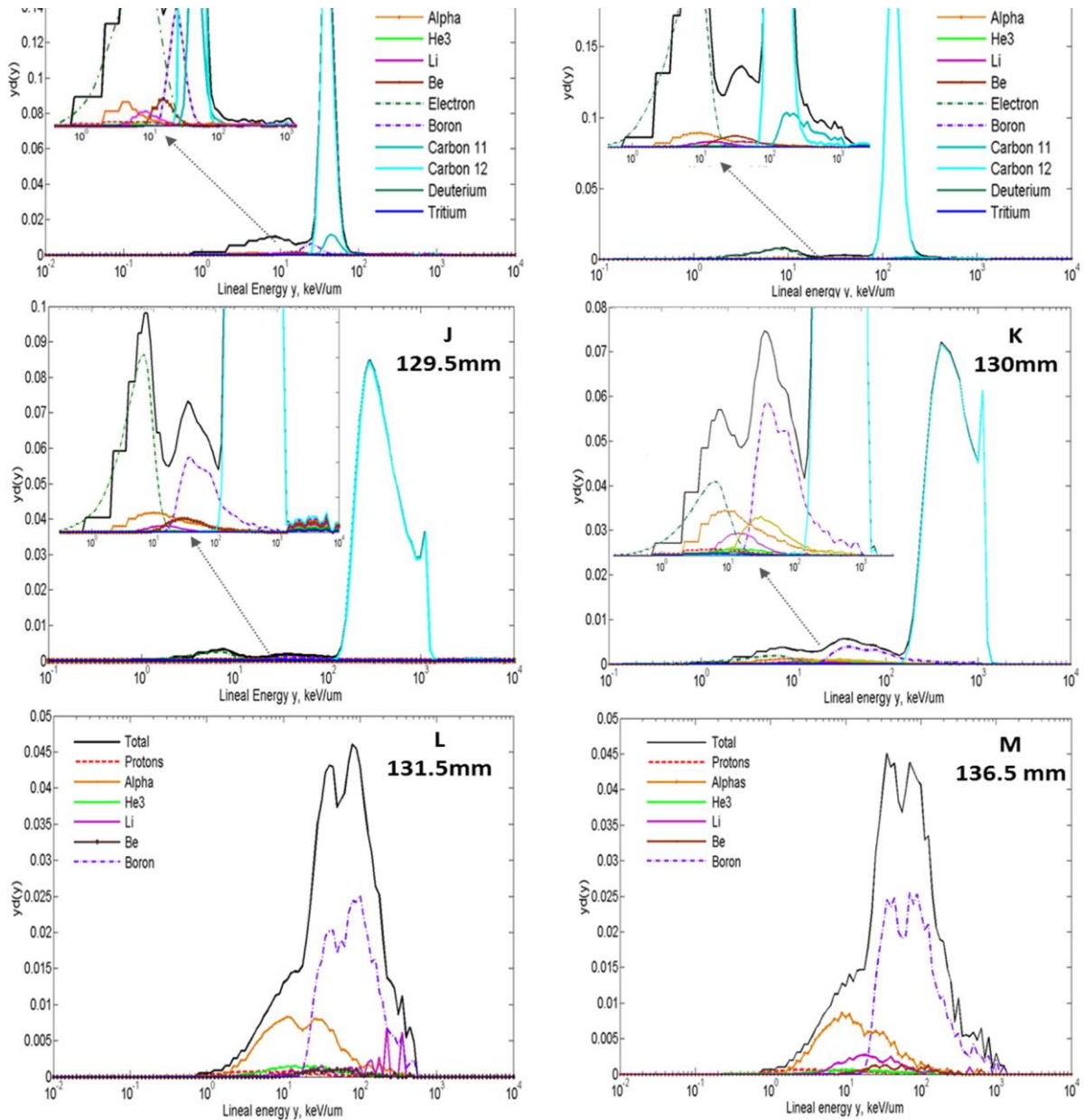
259 **Figure 7.** Response of  $\Delta E$ -E telescope to 290 MeV/u  $^{12}\text{C}$  ion at depths 0, 58, 128.5, 129.5, 130, 131.5 mm in the  
 260 PMMA phantom (two-dimensional  $\Delta E$ -E plot). The results are shown per incident particle.

261 The microdosimetric spectra in silicon (with area normalised to 1) measured by  $\Delta E$  stage in  
 262 response to 290 MeV/u  $^{12}\text{C}$  ion beam for depths of 106, 128.5, 129.5, 130 and 131.5 mm in the  
 263 PMMA phantom are shown in Fig. 8.

264 At all depths up to 130 mm, the dose weighted contribution from  $^{12}\text{C}$  ions was dominated with a  
 265 clear shifting of  $^{12}\text{C}$  microdosimetric spectrum to the region of higher lineal energies and spreading,  
 266 due to the  $^{12}\text{C}$  ion energy decreasing and  $^{12}\text{C}$  ion scattering and the energy straggling are increasing  
 267 with depth.

268 The other dose weighted partial microdosimetric spectra with lineal energies lower than 100  
 269 keV/ $\mu\text{m}$ , are corresponding to nuclear fragments such as B, Be, Li,  $^3\text{He}$ , alpha particles and protons.





270

271

**Figure 8.** Microdosimetric spectra derived from the  $\Delta E$  stage at positions D, I, J, K, L and M. Separated dose weighted components have been shown in each microdosimetric spectrum.

272

273

274

275

276

277

278

279

280

281

282

283

284

285

At a further depth in the PMMA phantom close to the distal part of the Bragg Peak (128.5 mm), a separate sharp peak occurs for the  $^{12}\text{C}$  dose weighted microdosimetric spectra which corresponds to  $^{12}\text{C}$  ions stopping in the  $\Delta E$  stage and having range of 1.8  $\mu\text{m}$  which is equal to the thickness of the  $\Delta E$  stage. This peak is more pronounced 0.5 mm further downstream at 130mm due to an increasing number of  $^{12}\text{C}$  ions with decreased energy at the very distal part of the BP. These detailed results demonstrate the capability of the silicon microdosimeter to obtain extremely high spatial resolution measurements, which were impossible with a TEPC, but which are crucial in determining the RBE accurately within the target tumor and beyond.

An interesting feature of the microdosimetric spectra is a partial dose weighted microdosimetric spectra peak corresponding to electrons. This peak is originated by scattered delta electrons from  $^{12}\text{C}$  ions. These electrons have energies below approximately 600 keV which is calculated using the formula:

$$E_{\text{electrons}} = (4m_e/M_{\text{ion}}) \cdot E_{\text{ion}}, \quad (5)$$

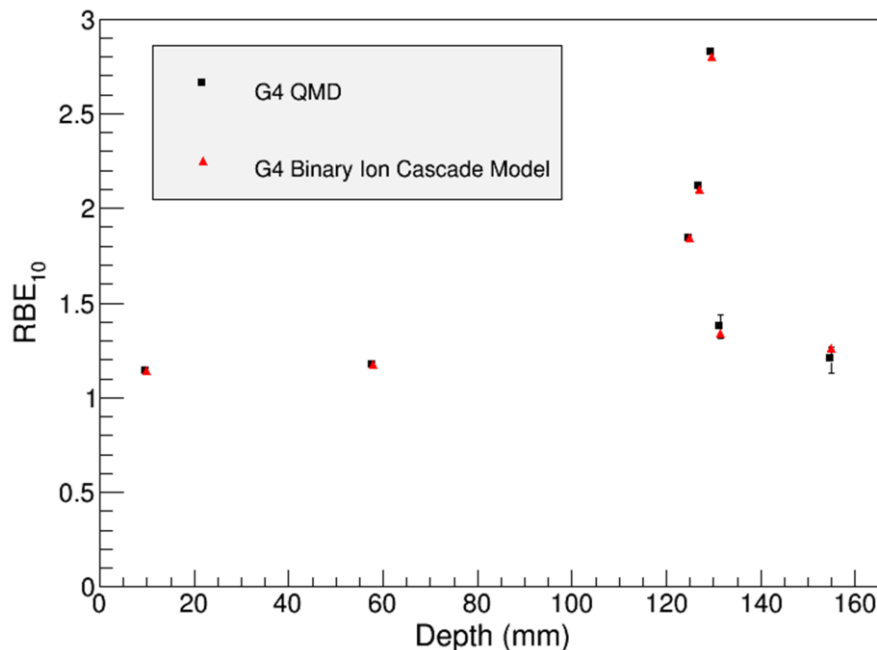
286 where  $m_e$  is the mass of electron,  $M_{ion}$  is the mass of carbon ions and  $E$  is the energy of the  $^{12}C$  ion.  
287 This peak is absent in the microdosimetric spectra at depth downstream of the Bragg peak that  
288 confirmed the origination of this peak.

289 Measurements of microdosimetric spectra at depth 131.5 mm (just behind of the Bragg peak) and  
290 136.5 mm along the distal part of the Bragg Peak shown in Fig. 8 indicated that primary  $^{12}C$  ions were  
291 not part of this mixed radiation field, although the contribution from fragments remains significant,  
292 with the largest dose weighted contribution deriving from B ions and alpha particles.

### 293 3.3 RBE derivation by the $\Delta E$ -E telescope in $^{12}C$ ion beam

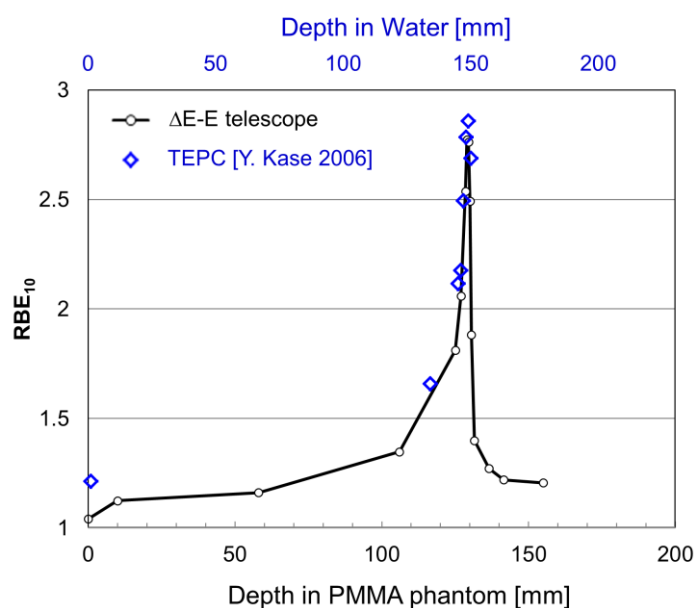
294 Using the microdosimetric spectra obtained by the  $\Delta E$  stage in response to 290 MeV/u  $^{12}C$  pristine  
295 BP for various depths in the PMMA phantom, the dose-mean lineal energy at each depth was  
296 obtained. The microdosimetric spectra have been converted from silicon to tissue using a conversion  
297 factor derived in [20].

298 The QGSP\_BIC\_HP physics list and the Quantum Molecular Dynamic (QMD) were used as  
299 alternative hadronic physics approaches to describe ion hadronic interactions. This strategy was  
300 adopted to evaluate the impact of alternative Geant4 physics models when calculating the  $RBE_{10}$ , by  
301 means of the MK model applied on the simulation microdosimetric results. Fig. 9 shows the  $RBE_{10}$   
302 profiles obtained with the two alternative physics models. The  $RBE_{10}$  values derived using the two  
303 models agreed well with one another within  $0.3 \pm 0.03\%$  in the proximal part of the BP,  $0.7 \pm 0.09\%$  at  
304 the BP and  $3.6 \pm 1\%$  in downstream of the BP.



305 **Figure 9:**  $RBE_{10}$  calculated adopting in the simulation the Geant4 Binary Ion Cascade and, alternatively, the  
306 QMD model, to describe ion hadronic interactions.  
307

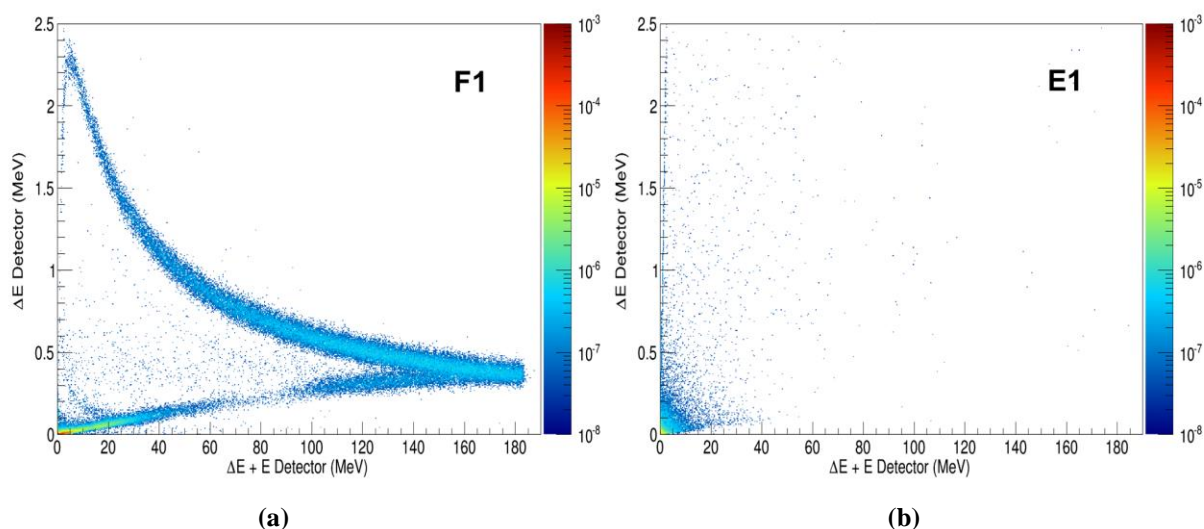
308 The  $RBE_{10}$  profiles calculated using the MK model obtained by means of the Geant4 simulation  
309 and experimentally using a TEPC are shown in Fig. 10. The maximum derived  $RBE_{10}$  found using the  
310  $1.8 \mu m$  thick  $\Delta E$  stage was approximately 2.8. The derived  $RBE_{10}$  profile, obtained by the  $\Delta E$  stage  
311 agrees well with the profile which was also calculated with MK model using microdosimetric spectra  
312 measured by a TEPC at NIRS, Japan [21], however a discrepancy was observed at an entrance depth  
313 where the TEPC was placed at 1 mm depth in water as presented in [21] and the  $\Delta E$ -E telescope was  
314 positioned at 0 mm depth in the PMMA phantom. This was due to the fact that the effective depth of  
315 the TEPC in water was actually 7.8 mm including the thickness of an A150 wall (1.27 mm), an Al  
316 shell (0.178mm) and physical size of the TEPC spherical volume (12.7 mm). It should be noted that  
317 the  $\Delta E$ -E telescope was measured in a PMMA phantom while the TEPC measurements were carried  
318 out in water, hence range scaling has been used to match the results.



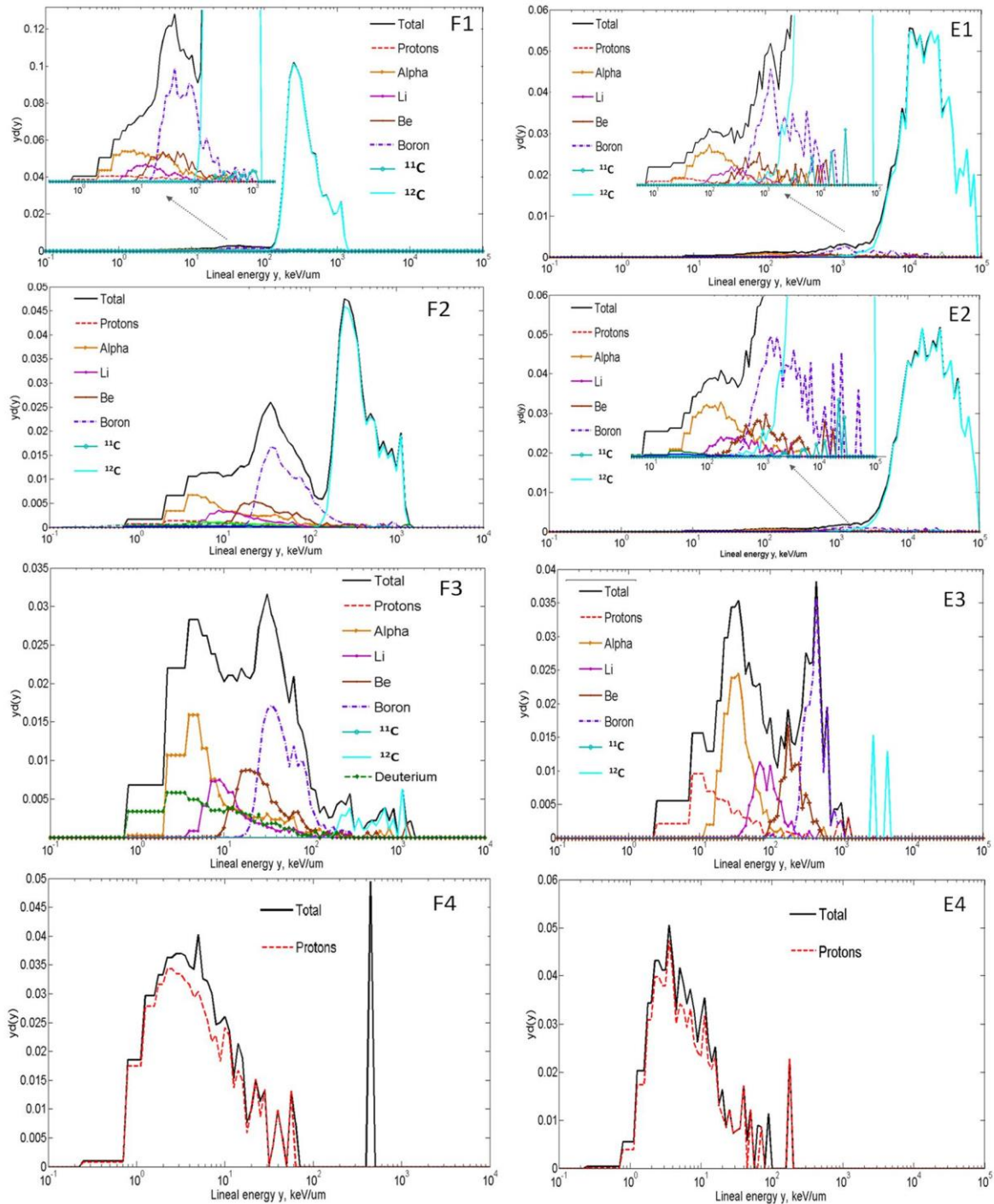
319  
 320 **Figure 10.** Derived  $RBE_{10}$  along the central axis of the  $^{12}\text{C}$  ion pristine BP, obtained by the  $\Delta E$  stage. The  
 321  $RBE_{10}$  derived from measured values of  $y^*$  [21] are shown by blue rotated square.

322 *3.4. Characterisation of  $\Delta E$ -E telescope response out of field*

323 Fig. 11 shows the response of the  $\Delta E$ -E telescope when the device was placed out-of-field laterally in  
 324 two configurations: face on ( $0^\circ$ ) and edge on ( $90^\circ$ ) (see Fig. 3). In the face on configuration there was a  
 325 clear loci that could distinguish different species of particles (Fig. 11 a) while the edge on  
 326 configuration revealed a very different 2D energy scatter plot with an absence of clear loci (Fig. 11 b);  
 327 this result indicated the preferable forward directionality of the out-of-field charged ion components.  
 328 The direction of the primary and secondary charged ions out-of-field can be seen in Fig. 5. The  
 329 absence of loci was due to the long path length of the particles coming through the  $\Delta E$  stage in edge-  
 330 on configuration. The observed scatter plot on Fig 11b is mostly due to delta electrons. Using  $\Delta E$  -E  
 331 telescope with pixelated  $\Delta E$  stage provided cylindrical well defined SVs that will minimize the  
 332 directional effect of the  $\Delta E$  stage used in microdosimetric mode, however, for identification of  
 333 particles, the  $\Delta E$ -E telescope should be in a face on positioning relative to the primary beam direction.  
 334



335  
 336 **Figure 11.** Response of the telescope detector when positioned out-of-field at 0mm.  $20 \times 10^6$  events were  
 337 simulated for both face on (F1) and edge on (E1) configurations. The results are shown per incident particle.  
 338



339  
340  
341  
342

**Figure 12.** Microdosimetric spectra derived from the  $\Delta E$  stage in out of field study at 0 mm, 2 mm, 7 mm and 47 mm from the edge of the beam at the Bragg peak. Separated components are shown in each microdosimetric spectrum.

343 Fig. 12 shows the microdosimetric spectra obtained by the  $\Delta E$  stage when the detector was placed  
344 face on at 0 mm, 2 mm, 7 mm, and 47 mm laterally from the edge of the beam (positions F1, F2, F3  
345 and F4), respectively, and edge on at positions E1, E2, E3 and E4 (see Fig. 3). When the  $\Delta E$ -E  
346 telescope was placed at 0 mm from the edge of the beam and the surface of the detector is facing the  
347 beam (F1 position), there was a significant contribution to the microdosimetric spectra from  $^{12}\text{C}$  ions  
348 that formed the penumbra region of the beam. Fragmentation products were also observed with lineal  
349 energies between a few  $\text{keV}/\mu\text{m}$  and  $100 \text{ keV}/\mu\text{m}$ , with the largest contribution coming from B ions.  
350 It is interesting that the dose weighted contribution from electrons was negligible due to lack of delta  
351 electrons originating from scattered Carbon ions in the penumbra region. At 2 mm from the edge of



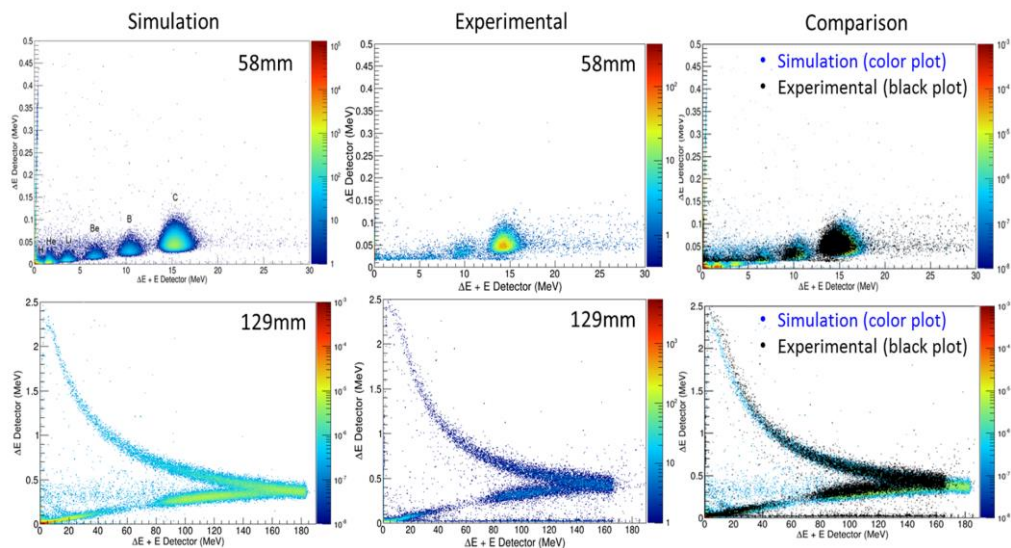
352 the beam (position F2), the partial dose weighted contribution of the  $^{12}\text{C}$  ions was reduced while the  
 353 contribution from fragments such as B, Be, Li, He, H increased. At 7 mm from the edge of the beam  
 354 (position F3) almost all  $^{12}\text{C}$  ions disappeared at this lateral depth but the fragments still remained  
 355 significant due to the sharp penumbra of the  $^{12}\text{C}$  ion beam. At a further lateral depth of 47 mm, only  
 356 protons which corresponded to the combination of fragmented and recoil protons generated from  
 357 neutron interactions in PMMA were observed.

358 A second alignment was carried out with the detector positioned in edge on configuration  
 359 (positions E1, E2, E3 and E4). Here more energy was deposited in the  $\Delta E$  stage from ions travelling  
 360 parallel to the side of the  $\Delta E$ -E detector. This caused a shift of microdosimetric spectra to the higher  
 361 lineal energies observed in E1-3 plots of Fig. 12, when a chord length of  $1.8\ \mu\text{m}$  was used. This shift  
 362 was clearer at positions closer to the field because nuclear fragments have a preferential forward  
 363 scattering angular trajectory from the originating ion, while the path along the  $\Delta E$  detector was 1 mm  
 364 long.

365 The microdosimetric spectra at 47 mm obtained by detector in edge on and face on configurations  
 366 are similar with most contribution from the protons originated by neutron elastic interactions in the  
 367 phantom with an isotropic distribution. A much closer agreement in the microdosimetric spectra for  
 368 positions F4 and E4 confirmed that the fragmented and neutron recoil proton fields were more  
 369 isotropic than other heavier fragmented ions that were scattered mostly along the beam. The results  
 370 showed that the microdosimetric spectra obtained by the  $\Delta E$  stage of the monolithic telescope can give  
 371 a detailed insight of the characteristics of the out of field beam. Certainly the microdosimetric spectra  
 372 presented for positions E1-3 should not be considered as radiobiologically relevant because of the  
 373 reasons cited above.

### 374 3.5. Comparison to experiment in HIMAC, Japan

375 Fig. 13 shows the experimental and the simulated response of the  $\Delta E$ -E telescope to  $290\ \text{MeV/u}$   $^{12}\text{C}$   
 376 ions in the PMMA phantom at 58 mm and 129 mm for the HIMAC beam line. At  $(58\pm 1)$  mm a good  
 377 agreement is observed between experimental measurements and simulation results. At  $(129\pm 1)$  mm  
 378 depth in the PMMA phantom, the maximum energy deposited in the E stage in the experiment was  
 379 about 160 MeV which is less than expected energy deposition in  $500\ \mu\text{m}$  of Si calculated by the  
 380 Geant4 simulation. This discrepancy can be explained by the plasma effect when high LET  $^{12}\text{C}$  ions  
 381 hit the E stage and produce dense electron-hole pairs called plasma columns. This leads to a strong  
 382 columnar recombination before drift charge collection is dominated because the electric field in  
 383 depleted E stage was not high enough. However, it can be clearly seen that the transmitted  $^{12}\text{C}$  ions  
 384 which have lower LET than  $^{12}\text{C}$  stoppers deposited the same energy as simulated starting from  
 385 approximately 80 MeV in both experimental and simulation results which supports the assumption  
 386 that the E stage is  $500\ \mu\text{m}$  thick and the charge deficit is due to phenomena described above.



387  
 388 **Figure 13.** Comparison of the simulated and experimental response of the  $\Delta E$ -E telescope, at the  $290\ \text{MeV/u}$   
 389  $^{12}\text{C}$  ion HIMAC therapeutic beam.



#### 390 4. Conclusion

391 The characterisation of the  $^{12}\text{C}$  ion beam at the HIMAC facility was studied in detail using Geant4.  
392 The 2D histogram of secondary charged particles provides very useful information about the  
393 distributions and directions of different ions of the mixed field.

394 The response of the  $\Delta\text{E-E}$  telescope to 290MeV/u  $^{12}\text{C}$  ion beam at various depths in the PMMA  
395 phantom at HIMAC facility was investigated theoretically and experimentally. The  $\text{RBE}_{10}$  values  
396 obtained by the  $\Delta\text{E-E}$  telescope were found to be in good agreement with values obtained using a  
397 TEPC. Due to the high spatial resolution of the 1.8  $\mu\text{m}$  thick  $\Delta\text{E}$  stage, more detailed measurements  
398 were obtained at the end of the Bragg Peak compared to the TEPC. One limitation affecting the  
399 reported comparison is that the TEPC measurements were carried out in water which lacks the carbon  
400 component in contrast to PMMA.

401 It has been demonstrated that using the silicon to tissue conversion factor one can convert the  
402 microdosimetric spectra from silicon to tissue.

403 This study demonstrated that the  $\Delta\text{E-E}$  silicon telescope can be used to characterise the mixed  
404 radiation field produced by the  $^{12}\text{C}$  therapeutic beam. It is also possible to simultaneously measure the  
405 microdosimetric spectra with high spatial resolution, which is not currently achievable using TEPCs.  
406 The microdosimetric spectra then can also be used to determine the  $\text{RBE}_{10}$  of the radiation field by  
407 means of the MK model.

408 The  $\Delta\text{E-E}$  telescope can be used to improve the Quality Assurance of existing treatment planning  
409 systems used in Heavy Ion Therapy and Geant4 benchmarking.

410 This study showed that adopting the G4IonBinaryCascade or, alternatively, the Geant4 QMD  
411 model does not have a significant impact on the calculation of the  $\text{RBE}_{10}$ .

412 Good agreement has been observed between simulation and experimental results, however a more  
413 in depth, systematic, quantitative comparison is foreseen as a next stage of the project, to quantify the  
414 accuracy of the Geant4 simulation model, using alternative hadronic physics models for ions. The  
415 experimental results concerning the response of the monolithic and pixelated  $\Delta\text{E-E}$  telescope in the  
416 290 MeV/u  $^{12}\text{C}$  ion beam at HIMAC will be presented in more detail in a future paper.  
417

#### 418 5. Acknowledgement

419 We would like to thank the University of Wollongong Information Technology Services (ITS) for  
420 computing time on the UOW High Performance Computing Cluster and the research centre for charge  
421 particle therapy, National Institute of Radiological Science, Japan for providing valuable  $^{12}\text{C}$  ion  
422 beam.

#### 423 References

- 424 [1] Bethe, H., "Theory of the Passage of Fast Corpuscular Rays Through Matter" *Ann. Phys.*, 397,  
425 325-400, 1930  
426 [2] Bloch F., "Bremsvermogen von Atomen mit mehreren Elektronen", *Z. Phys.*, 81, 363-376, 1933  
427 [3] PART III. "Particles and Radiation Therapy, Third International Conference," *Int. J. Radiat. Oncol.*  
428 *Biol. Phys.*, 8 (1982).  
429 [4] Matsufuji N, Kanai T, Kanematsu N, Miyamoto T, Baba M, Kamada T, Kato H, Yamada S, Mizoe  
430 JE, Tsujii H 2007 Specification of Carbon Ion Dose at the National Institute of Radiological  
431 Sciences (NIRS). *Journal Radiation Research*, 48 Suppl. A:A81-6.  
432 [5] Rossi and M. Zaider 1996 Microdosimetry and its Applications. *London: Springer*.  
433 [6] Y. Kase, T. Kanai, M. Sakama, Y. Tameshige, T. Himukai, H. Nose, N. Matsufuji 2011  
434 Microdosimetric Approach to NIRS-defined Biological Dose Measurement for Carbon-ion  
435 Treatment Beam, *Journal of Radiation Research*; ISSN:0449-3060; Vol.52; No.1; Page. 59-68;  
436 [7] A. B. Rosenfeld, "Novel detectors for silicon based microdosimetry, their concepts and  
437 applications," *Nucl. Instrum. Meth., Phys. Res. A*, vol. 809, pp. 156–170, February 2016.  
438 [8] E Haettner, H Iwase, M Krämer, G Kraft and D Schardt, 2013 Experimental study of nuclear  
439 fragmentation of 200 and 400 MeV/u  $^{12}\text{C}$  ions in water for applications in particle therapy *Physics*  
440 *Medicine Biology*. 58 8265 doi:10.1088/0031-9155/58/23/8265

- 441 [9] H. Matsumoto, H. Koshiishi, T. Goka, M. Fujii, M. Hareyama, N. Kajiwara, S. Kodaira, K.  
442 Sakurai, N. Hasebe 2005 Delta ExE silicon telescope of energetic heavy ions trapped in radiation  
443 belts, *Japanese Journal Applied Physics*, Part 1 44(9A), 6870–6872.
- 444 [10] A. J. Kordyasz, E. Nossarzewska-Orlowska, E. Piaseckic, D. Lipiński, A. Brzozowski, J.  
445 Kownacki, M. Kowalczyk, Ł. Świdorski, A. Syntfeld, L. Reissig, A. Pietrzaa, A. Jakubowski, R.  
446 Pozoreka, R. Gąsiorowski 2004 Response to heavy ions and fission fragments of the monolithic  
447 silicon E-delta E telescopes produced by the quasiselective epitaxy, *Nuclear Instruments Methods*  
448 *in Physics Research A* **530**, 1–2, 87–91.
- 449 [11] L. T. Tran, L. Chartier, D. A. Prokopovich, M. I. Reinhard, M. Petasecca, S. Guatelli, M. L. F.  
450 Lerch, V. L. Perevertaylo, M. Zaider, N. Matsufuji, M. Jackson, M. Nancarrow, and A. B.  
451 Rosenfeld, 2014 3D-Mesa “Bridge” Silicon Microdosimeter: Charge Collection Study and  
452 application to RBE Studies in <sup>12</sup>C Radiation Therapy. *IEEE Trans. Nucl. Sci.* Vol. 62(2), (2015)  
453 504-511.
- 454 [12] S. Agosteo, P.G. Fallica, A. Fazzi, M.V. Introini, A. Pola, G. Valvo 2008 A pixelated silicon  
455 telescope for solid state microdosimetry, *Radiation Measurement*, 43, 585-589.
- 456 [13] Andrew Wroe, Reinhard Schulte, Alberto Fazzi, Andrea Pola, Stefano Agosteo, Anatoly  
457 Rosenfeld, 2009 Direct RBE estimation of radiation fields using a ΔE-E telescope (*Medical*  
458 *Physics*, 36 (10) (2009) 4486-4494.
- 459 [14] Linh T. Tran Lachlan Chartier, David Bolst, Alex Pogosso, Susanna Guatelli, Dale A.  
460 Prokopovich, Marco Petasecca, Michael L. F. Lerch, Mark I. Reinhard, Benjamin Clasio, Nicolas  
461 Depauw, Hanne Kooy, Jay Flanz, Aimee McNamara, Harald Paganetti, Chris Beltran, Keith  
462 Furutani, Vladimir L. Perevertaylo, Michael Jackson and Anatoly B. Rosenfeld. “Characterisation  
463 of proton pencil-beam scanning using a high spatial resolution solid state microdosimeter”,  
464 *Medical Physics*, doi: 10.1002/mp.12563, 2017.
- 465 [15] Geant4 Collaboration 2012 Geant4 User’s Guide for Application Developers
- 466 [16] ICRU 1989 Tissue Substitutes in Radiation Dosimetry and Measurement, (Report 44 of the  
467 *International Commission on Radiation Units and Measurements*).
- 468 [17] J. Allison et al. Geant4 Collaboration 2006 Geant4 Developments and Applications, *IEEE*  
469 *Transactions on Nuclear Science*, vol. 53 (1), pp. 270-278.
- 470 [18] NIST, National Institute of Standards and Technology PSTAR Database Program  
471 <http://physics.nist.gov/cgi-bin/Star/compos.pl?ap>.
- 472 [19] J. F. Ziegler, SRIM 2008 [Online]. Available: <http://www.srim.org>
- 473 [20] D. Bolst, S. Guatelli, L. T. Tran, L. Chartier, M. Lerch, N. Matsufuji and A. Rosenfeld,  
474 “Correction factors to convert microdosimetry measurements in silicon to tissue in <sup>12</sup>C ion  
475 therapy,” *Phys. Med. Biol.*, vol. 62, no. 6, pp. 2055-2069, 2017.
- 476 [21] Y. Kase, T. Kanai, Y. Matsumoto, Y. Furusawa, H. Okamoto, T. Asaba, M. Sakama, and H.  
477 Shinoda, 2006 Microdosimetric Measurements and Estimation of Human Cell Survival for Heavy-  
478 Ion Beams. *Radiation Research*, Vol. 166, No. 4, pp. 629-638.